Catalysis Science & Technology

ROYAL SOCIETY OF CHEMISTRY

PAPER

View Article Online
View Journal | View Issue

Cite this: *Catal. Sci. Technol.*, 2024, **14**, 2541

Sulfur substitution in Fe-MOF-74: implications for electrocatalytic CO_2 and CO reduction from an *ab initio* perspective†

Gavin A. McCarver, * Taner Yildirim and Wei Zhou

Employing first-principles methods, we investigated the electrocatalytic reduction of CO_2 and CO on two Fe-based MOFs: Fe_2DOBDC and Fe_2DSBDC. Our primary objective was to discern the impact of substituting S atoms into the framework while maintaining the topological structure. We anticipated significant changes in reduction reactions due to differences in chemical properties such as electronegativity, atomic radius, polarizability, and charge density upon replacing O atoms with S atoms. Atomic charge analysis highlights some of these differences by showing the equatorial Fe–O/S bonds of Fe_2DSBDC are less polarized and result in smaller positive and negative charges on the Fe and O/S atoms, respectively. Additionally, the larger S atoms are expected to weaken adsorbate binding due to less favorable van der Waals interactions near the open-metal Fe site. Consequently, the less electropositive Fe site and the larger S atoms of Fe_2DSBDC impede the adsorption of reduced CO_2 and CO products, while the more electropositive Fe site and smaller O atoms of Fe_2DOBDC strongly favor product adsorption. Specifically, the weak binding of HCOOH and CH_2O intermediates on Fe_2DOBDC (ΔG of −0.07 eV and −0.11 eV, respectively) indicates feasible further reduction to CH_2O and CH_4 for CO_2RR and CORR, respectively. Conversely, these adsorbates exhibit unfavorable binding to the Fe site of Fe_2DSBDC (ΔG of +0.14 eV and +0.25 eV, respectively), limiting further reduction possibilities. Thus, CO_2 and CO reduction on Fe_2DSBDC are likely to yield only $2e^-$ products (HCOOH and CH_2O, respectively), whereas Fe_2DOBDC is expected to produce deeper reduction products (CH_2O and CH_4, respectively). Additionally, significant differences in free energy for the first reduction steps post-sulfur substitution indicate more favorable energetics for both CO_2 and CO reductions (ΔG = −0.12 eV and −0.58 eV, respectively). These findings lay the groundwork for designing novel MOFs with tunable reaction behaviors by strategically replacing O atoms with heavier S atoms in the MOF scaffold.

Received 16th February 2024,
Accepted 20th March 2024

DOI: 10.1039/d4cy00217b

rsc.li/catalysis

1 Introduction

The conversion of carbon dioxide (CO_2) and carbon monoxide (CO) into higher-value fuels, feedstock materials, and fine chemicals stands at the forefront of extensive research endeavors, offering a promising approach to diminish our dependence on fossil fuels.[1–3] Electrocatalysis, a versatile process adept at reducing both CO_2[4,5] and CO[5,6] has emerged as a vital technique for converting these molecules into more value-added materials. Within this landscape, metal–organic frameworks (MOFs), a burgeoning class of materials, exhibit significant potential for electrocatalytic reduction reactions.[7] These coordination polymers, featuring metal nodes coordinated to organic linkers, boast uniform and well-characterized active sites akin to traditional homogeneous catalysts while maintaining a heterogeneous structure, effectively bridging the catalytic realms.[8]

Identifying and synthesizing MOFs with potential as electrocatalysts for reduction reactions presents a considerable challenge, demanding materials with intrinsic charge-carrying capabilities to facilitate essential electron transfer during reduction processes.[9,10] To illustrate, Sun and

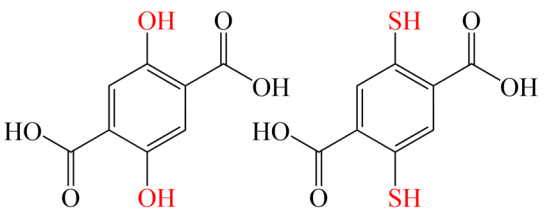

Fig. 1 Molecular structures of the DOBDC (left) and DSBDC (right) ligands used to construct the Fe_2DOBDC and Fe_2DSBDC MOFs, respectively.

National Institute of Standards and Technology, Center for Neutron Research, Gaithersburg, Maryland 20899-6102, USA. E-mail: gavin.mccarver@nist.gov

† Electronic supplementary information (ESI) available: Reaction energetics and Cartesian coordinates for each reactant, intermediate, and product. See DOI: https://doi.org/10.1039/d4cy00217b

colleagues demonstrated a notable breakthrough in enhancing the electrical conductivity of Fe-MOF-74 (Fe_2-DOBDC, DOBDC = 2,5-dihydroxybenzene-1,4-dicarboxylate, Fig. 1).[11] They achieved this by introducing thiophenoxide groups through the replacement of phenoxide groups, utilizing 2,5-disulfhydrybenzene-1,4-dicarboxylate (DSBDC). This modification resulted in an increased electrical conductivity without altering the well-established MOF-74 topology, now featuring $(–Fe–S–)_\infty$ chains. The significant improvement in electrical properties was attributed to the presence of the heavier chalcogenide atoms. This aligns with the historical chemistry of organic conductors, where such elements typically contribute to enhancements in electrical conductivity.[12] Additionally, recent work by Ali *et al.* have shown the utility of sulfur substitution in MOFs to modify the CO_2 reduction reaction.[13,14]

In light of the enhanced electrical conductivity observed in Fe_2DSBDC, we aimed to expand upon our earlier theoretical exploration focused on X-MOF-74 (X = Mg, Mn, Fe, Co, Ni, Cu, Zn) for the reduction of CO_2.[15] Our previous work addressed the unexplored realm of CO_2 reduction on Fe-MOF-74, a system that has not been previously studied either experimentally or computationally for this specific purpose. In this investigation, Fe-MOF-74 demonstrated substantial promise for CO_2 reduction, showcasing strong binding of reduced intermediates to limit desorption and push the reduction completely towards methane (CH_4) formation, a low limiting potential (0.32 eV), and a favorable selectivity for CO_2 reduction over hydrogen reduction. Given that both the Fe_2DOBDC and Fe_2DSBDC materials share an identical topological structure, delving into how the introduction of heavier chalcogenide atoms might influence the reduction of both CO_2 and CO became imperative.

The introduction of S atoms in DSBDC brings about several distinct properties that can significantly influence catalytic reactivity for these reduction reactions. Firstly, the lower electronegativity of S atoms (2.659) compared to O atoms (3.758)[16] results in a less pronounced bond polarity between Fe and S atoms. Additionally, the larger, softer S atoms possess lower charge density and higher polarizability than the harder O atoms, contributing to distinct chemical interactions.[17] Furthermore, the larger S atoms might induce increased repulsive van der Waals interactions between the Fe site and adsorbate molecules.[18] Lastly, differing orbital interactions between Fe and O *versus* Fe and S atoms contribute to a larger band gap of 1.92 eV in Fe_2DSBDC compared to the 1.47 eV band gap in Fe_2DOBDC, potentially leading to notable differences for reduction reactions.[11] This presents an opportunity to finely adjust these reactions based solely on the presence or absence of the heavier S atoms, adding a layer of versatility of these promising materials.

Given the well-known reactivity of Fe centers in Fe_2-DOBDC,[19] electrochemical reduction reactions might present experimental challenges. Moreover, the stability of many MOFs in solvated conditions is a crucial consideration. Therefore, it is imperative to ensure the stability of both Fe_2-DOBDC and Fe_2DSBDC materials under solvated and electrochemical conditions. Previous studies by Van Phuc *et al.*[20] and Choi *et al.*[21] have thoroughly examined the stability and applicability of X-MOF-74 materials (where X = Co, Ni, Cu, Zn) under electrochemical conditions using 0.1–0.5 M $KHCO_3$ as the electrolyte. Furthermore, there is abundant literature evidence of Fe-based catalysts being employed for CO_2 reduction reactions under DMF, the same solvent used during the synthesis of Fe_2DOBDC and Fe_2-DSBDC by Sun *et al.*[11] Hence, these studies collectively suggest that the Fe_2DOBDC and Fe_2DSBDC materials should demonstrate stability under electrochemical conditions and DMF solvation.

Our results highlight distinctive chemical behaviors arising from the Fe–O and Fe–S bonds in Fe_2DOBDC and Fe_2DSBDC, respectively, underscoring the significant variations in their responses to closed-shell products from CO_2 and CO reduction. We also study the reduction of hydrogen on these materials as this reaction often competes with other reduction reactions in acidic solutions. The Fe_2-DOBDC MOF exhibits heightened affinity for reduced CO_2 and CO intermediates, fostering the formation of more deeply reduced products, including CH_2O (formaldehyde) and CH_4. In contrast, the Fe_2DSBDC MOF results in weakened interactions with closed-shell reactants, intermediates, and end products. We attribute this behavior to the larger size of the S atoms resulting in less favorable interactions and the less polarized equatorial Fe–O/S bonds which result in a less electropositive Fe site. Consequently, Fe_2DSBDC predominately yields $2e^-$ reduced products, specifically HCOOH (formic acid) and CH_2O, following CO_2 and CO reduction, respectively (see Table 1 for equilibrium potentials).[22] Notably, the limiting potential for CO_2 reduction remains consistent across the various ligand backbones, while CO reduction exhibits significant changes in limiting potential. These outcomes underscore the substantial influence of the ligand's identity within the MOF scaffold, shaping the products emerging from CO_2 and CO reduction, and highlighting the pivotal role of metal–ligand binding disparities. This study not only sheds light on the distinctive metal–ligand binding interactions in Fe_2DOBDC and Fe_2DSBDC but also provides a framework for the strategic engineering of other MOFs, aiming to uncover novel metal–ligand interactions that could impart significant variations in reactivities for diverse reduction reactions.

Table 1 Electrochemical reactions with equilibrium potentials

Reaction	E^0/[V *vs.* RHE]
$CO_2 + 2H^+ + 2e^- \rightarrow HCOOH$	−0.61
$CO_2 + 2H^+ + 2e^- \rightarrow CO + H_2O$	−0.53
$CO_2 + 4H^+ + 4e^- \rightarrow CH_2O + H_2O$	−0.48
$CO + 6H^+ + 6e^- \rightarrow CH_4 + H_2O$	0.26

2 Computational details

In the investigation of the Fe_2DOBDC and Fe_2DSBDC materials, we use two cluster models to investigate the CO_2 and CO reduction reactions at the open metal sites. Our justification for using cluster models instead of fully periodic systems lies in the extensive prior literature examining MOF-74 in particular and MOFs in general for different applications.[23] Our chosen cluster model for MOF-74 follows previous work conducted by Verma and colleagues.[24] Each MOF was represented by an 88-atom section, comprising three Fe sites and six DEBDC (E = O, S) ligands. Dangling valencies were appropriately capped to maintain a neutral charge. Additionally, each Fe site was coordinated with a DMF ligand, effectively simulating the first solvation shell. Fig. 2 shows representations of the models for Fe_2DOBDC and Fe_2DSBDC, respectively.

Our computational protocol follows our prior research on the utilization of cluster models of MOFs for catalytic reduction reactions.[15,25] We employed the M06L[26] density functional with D3zero dispersion corrections,[27] as implemented in ORCA version 5.0.3.[28] Standard SCF and optimization criteria were maintained, and unrestricted Kohn–Sham wave-functions were assumed for all calculations. The central Fe atom was assigned using the def2-TZVPP basis set, the first coordination sphere around the central Fe atom and adsorbate atoms were assigned the def2-TZVP basis set, and all other atoms were assigned the def2-SV(P) basis set.[29] Furthermore, we employed the resolution of identity (RI)[30] method to accelerate the computation of four-index integrals using the def2/J auxiliary basis set.[31] Implicit solvent effects were included *via* the conductor-like polarizable continuum model (CPCM), utilizing DMF as the solvent.[32] Charge model 5 (CM5) atomic charges[33] and other properties are calculated using the Multiwfn program.[34] Orbital localization is performed using the Pipek–Mezey method[35] and visualized with Iboview.[36,37]

The free energy (G) of each reactant, intermediate, and product is the basis for our energy calculations, and is determined according to:

$$G = E + I + H - TS - eU \quad (1)$$

Here, E represents the total electronic energy, I comprises the total internal energy, including zero-point and thermal energies, and H and S denote the enthalpy and entropy, respectively, calculated at a temperature (T) of 298.15 K. These values are calculated following an analytical frequency calculation using the quasi-rigid rotor harmonic oscillator (Quasi-RRHO) approximation.[38] Lastly, eU is the effect of an applied potential U for each elementary step (e). We assumed that each reduction step proceeds through a proton-coupled electron transfer (PCET) mechanism as an initial approximation.[39,40] Essentially, this involves the addition of a hydrogen atom as a H^+/e^- pair in each elementary step of the reaction. The reaction energy of each step of the reduction reaction are referenced relative to the energy of the MOF cluster, a CO_2 molecule, and a varying number of H^+/e^- pairs, depending on the number of PCET steps that have occurred. We considered the energy of a single H^+/e^- pair as 1/2 the energy of an H_2 molecule, following the computational hydrogen electrode (CHE) model.[41] The limiting potential for each closed-shell product is determined as the highest free energy difference (ΔG_{max}) between two elementary steps of the reaction.

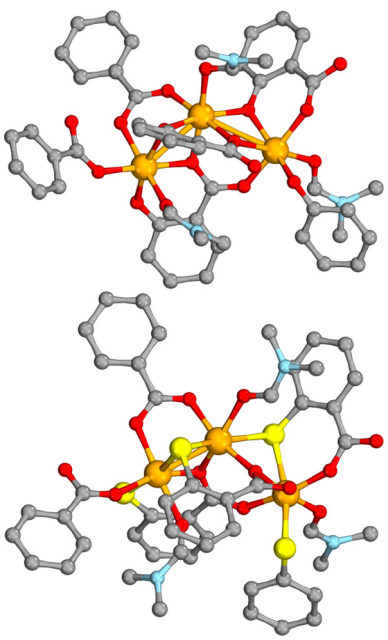

Fig. 2 Cluster models for the Fe_2DOBDC (top) and Fe_2DSBDC (bottom) MOFs. Hydrogen atoms removed for clarity. Color code: C (grey), N (blue), O (red), S (yellow), Fe (orange).

3 Results & discussion

3.1 Electronic structure of Fe_2DOBDC and Fe_2DSBDC clusters

Electronic structure disparities between the Fe_2DOBDC and Fe_2DSBDC clusters are evident across various properties, notably the atomic charges of the Fe atoms. Significant differences emerge, with values of 0.63 and 0.48 for Fe_2-DOBDC and Fe_2DSBDC, respectively (Table 2). The introduction of the heavier chalcogenides results in a more

Table 2 CM5 atomic charges of the neutral and singly-reduced Fe_2-DOBDC and Fe_2DSBDC clusters[a]

	Fe_2DOBDC	$[Fe_2DOBDC]^-$	Fe_2DSBDC	$[Fe_2DSBDC]^-$
Fe	0.63	0.57	0.48	0.45
O_{ax}	−0.36	−0.35	−0.36	−0.36
O_{eq}/S_{eq}	−0.35	−0.45	−0.27	−0.32
O_{DMF}	−0.34	−0.33	−0.33	−0.32

[a] O_{ax} denotes the axial O atom, O_{eq}/S_{eq} represents the average atomic charges of the O and/or S equatorial atoms, and O_{DMF} pertains to the O atom of the adsorbed DMF molecule.

diminished positive charge on the Fe center, counteracted by less negatively charged equatorial atoms (both O and S). In Fe_2DOBDC, the average atomic charge for the four equatorial O atoms is −0.35, while in Fe_2DSBDC, the equatorial O and S atoms show an average atomic charge of −0.27. These distinctions between the Fe centers and the equatorial atoms suggest a higher bond polarity in the Fe_2DOBDC cluster compared to Fe_2DSBDC. This contrast becomes more pronounced following reduction through the addition of an electron to the cluster. The charge of the Fe centers undergoes minimal change (to 0.57 and 0.45 for Fe_2DOBDC and Fe_2DSBDC, respectively), indicating the unlikelihood of the additional electron residing on the Fe centers. In contrast, the equatorial O atoms of Fe_2DOBDC become more negatively charged by an average of −0.10, while the O and S equatorial atoms of Fe_2DSBDC exhibit a smaller change of −0.05. These trends imply that the Fe_2DSBDC material should demonstrate enhanced electrical conductivity due to the greater electron delocalization within the cluster, aligning with the findings of Sun *et al.*[11]

In both Fe_2DOBDC and Fe_2DSBDC clusters, each Fe center is presumed to adopt a high-spin, S = 2 quintet spin configuration, as established in prior studies.[24] This configuration gives rise to a single β electron in the d-orbitals of each Fe center, a characteristic attributed by Sun *et al.*[11] to the high electrical conductivity of these materials. The molecular orbitals where these β electrons reside exhibit considerable overlap among the Fe centers for the Fe_2DSBDC cluster while little overlap is observed for the Fe_2DOBDC cluster (Fig. S1†). This heightened orbital overlap, in conjunction with the $(–Fe–S–)_\infty$ chains, likely contributes to the superior electrical conductivity observed in the Fe_2DSBDC material. Anticipated variations in the reduction reactions' performance between the two materials stem from these electronic structure differences.

The initial step of the reduction reactions involves activation through solvent removal. On neutral clusters, this process is unfavorable, with ΔG values of 0.39 eV and 0.14 eV for Fe_2-DOBDC and Fe_2DSBDC, respectively. However, upon reduction, the removal of the DMF adsorbate becomes slightly favorable (ΔG = −0.09 eV) on the Fe_2DOBDC cluster and more favorable (ΔG = −0.25 eV) on the Fe_2DSBDC cluster. For simplicity, we will describe each elementary step of the reduction reaction, assuming a PCET mechanism, as quantifying the free energy of a proton using DFT is challenging. However, we will discuss the activation of CO_2 on the singly reduced clusters to evaluate the activation barrier (as discussed below).

3.2 Hydrogen evolution reaction (HER)

As hydrogen reduction often competes with other reduction reactions in acidic solutions, it is essential to explore on any new catalyst to assess the interplay between these processes. Due to the softer nature of sulfur atoms within Fe_2DSBDC, we conducted tests on hydrogen adsorption at these sites. However, we observed that adsorption was less favorable on the sulfur sites compared to the Fe site by 0.12 eV. The formation of *H species at the Fe sites of Fe_2DOBDC and Fe_2DSBDC clusters results in nearly identical formation energies of 1.30 eV and 1.31 eV, respectively (as illustrated in Fig. S2 and S3†). Here, the * symbol indicates surface adsorption of the intermediate. Similarly, the Fe–H bond lengths are consistent at 1.54 Å in both clusters, and the localized MOs composed of the Fe–H bond exhibit orbital energies of −0.25 eV (refer to Fig. S4†). A slight decrease in the atomic charge of the Fe centers of approximately −0.10 is observed following the formation of the Fe–H intermediates, while the hydrogen atoms remain slightly negatively charged at −0.12 for both clusters. Furthermore, the H_2 molecule formed following a second PCET step shows weak physisorption to the Fe centers, with binding energies of 0.11 eV and 0.00 eV for Fe_2DOBDC and Fe_2DSBDC, respectively. Consequently, despite significant electronic structure differences between the Fe_2DOBDC and Fe_2DSBDC clusters, the reduction of hydrogen is anticipated to follow nearly identical energetics with limiting potentials of approximately 1.30 eV.

3.3 CO_2 reduction reaction (CO_2RR)

The adsorption and subsequent activation of CO_2 following an initial reduction of the clusters exhibit significant variations depending on the presence or absence of the S atoms in the MOF clusters. Weak physisorption is observed for CO_2 on both clusters with an O-oriented binding motif (Fig. 3a and d), and there is little to no change in the atomic charges of the atoms of the CO_2 molecules (Table 3). After adsorption, the activation of CO_2 proceeds through a single transition state where one of the C═O double bonds is broken. On the Fe_2DOBDC cluster, this transition state (Fig. 3b) occurs with a barrier of 0.14 eV (3.3 kcal mol^{-1}),

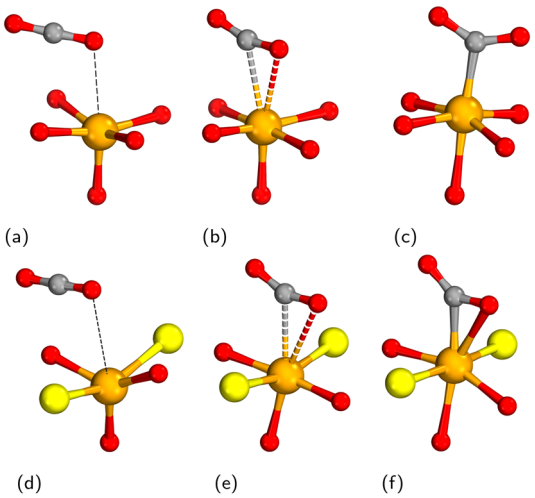

Fig. 3 Molecular structures depicting the first coordination sphere of the Fe_2DOBDC (top row) and Fe_2DSBDC (bottom row) clusters following adsorption and activation of CO_2. Physisorbed CO_2 shown in (a) and (d), the transition state is depicted in (b) and (e), and the fully activated complex is shown in (c) and (f). Color code: C (grey), O (red), S (yellow), Fe (orange).

Table 3 CM5 atomic charges (q), inter-atomic distances (R, Å), and bond angles (A, °) for CO_2 activation[a]

	Fe_2DOBDC				Fe_2DSBDC		
	CO_2	$*CO_2$	$*CO_2^{\ddagger}$	*OCO	$*CO_2$	$*CO_2^{\ddagger}$	*OCO
q_{O^1}	−0.21	−0.19	−0.26	−0.38	−0.21	−0.27	−0.33
q_C	0.43	0.42	0.32	0.10	0.40	0.27	0.14
q_{O^2}	−0.21	−0.21	−0.24	−0.39	−0.21	−0.29	−0.37
$\sum q_{CO_2}$	0.01	0.02	−0.18	−0.67	0.02	−0.29	−0.56
R_{Fe-O^1}	—	2.684	2.548	2.802	4.171	3.212	2.971
R_{Fe-C}	—	3.147	2.529	2.051	3.919	2.516	2.069
R_{Fe-O^2}	—	3.933	3.311	2.697	4.037	2.802	2.448
R_{C-O^1}	1.159	1.163	1.187	1.228	1.160	1.185	1.211
R_{C-O^2}	1.159	1.157	1.176	1.231	1.160	1.194	1.232
$A_{O^1-C-O^2}$	180.0	178.1	160.1	137.0	178.1	153.4	139.9

[a] $*CO_2^{\ddagger}$ refers to the transition state associated with CO_2 activation and *OCO refers to the fully activated CO_2 complex. O^1 and O^2 refer to the O atoms furthest from and closest to the Fe site, respectively.

coinciding with an accumulation of charge of −0.18 on the CO_2 adsorbate. The C atom of the transition state becomes less positively charged (from 0.42 to 0.32) while the O atoms each become more negatively charged. Activation of CO_2 on Fe_2DSBDC (Fig. 3e) occurs with a activation barrier of 0.74 eV (17.0 kcal mol^{-1}) which is significantly higher than on the Fe_2DOBDC cluster. This transition state results in a greater amount of charge accumulation on the CO_2 adsorbate of −0.29, possibly due to the more facile charge delocalization of the Fe_2DSBDC cluster. The low barrier for CO_2 activation on the Fe_2DOBDC cluster may indicate that CO_2 reduction will be more readily achieved than on the Fe_2DSBDC cluster based on the chemical kinetics.

The initial PCET step for CO_2 reduction on the neutral Fe-MOF clusters favors the formation of the *OCHO intermediate *via* C atom reduction over the formation of the *OCOH intermediate following O atom reduction (Fig. 4). As with hydrogen reduction, we investigated the relative difference between *OCHO formation on the S and Fe sites of Fe_2DSBDC. We found a large difference of 0.92 eV, indicating more favorable reduction on the Fe sites. The difference in free energy between the formation of *OCHO and *OCOH intermediates is more significant on the Fe_2DSBDC cluster, with a value of −0.64 eV, compared to −0.33 eV on the Fe_2-DOBDC cluster. This energetic preference for the *OCHO intermediate may arise from greater amount of orbital stabilization through the Fe–O bonds as opposed to the Fe–C bonds. The molecular orbitals for the *OCHO intermediates primarily consist of O p-orbitals donating electron density into the empty Fe p- and d-orbitals, while the *OCOH intermediates result in molecular orbitals that are composed of a combination of C p-orbitals and Fe d-orbitals (Fig. S5†). The reaction energetics for the first PCET step are remarkably close between the two clusters, with Fe_2DOBDC requiring 1.14 eV while Fe_2DSBDC requires 1.02 eV. These results resemble those observed for hydrogen reduction, indicating that some of the

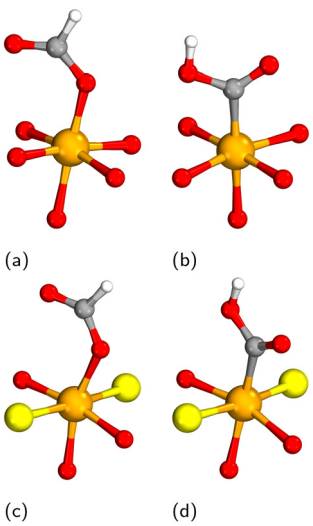

Fig. 4 Molecular structures depicting the first coordination sphere of the Fe_2DOBDC (top row) and Fe_2DSBDC (bottom row) clusters following the first PCET step to form *OCHO (a and c) and *OCOH (b and d). Color code: H (white), C (grey), O (red), S (yellow), Fe (orange).

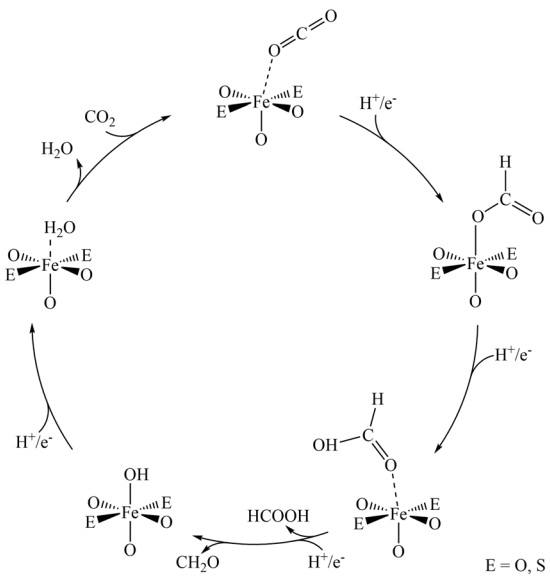

Fig. 5 Mechanistic cycle for the reduction of CO_2 to HCOOH and CH_2O. E = O or S for Fe_2DOBDC or Fe_2DSBDC, respectively.

reduction steps proceed with similar energetics given the different MOF clusters.

A subsequent PCET step on both clusters strongly favors the formation of *HCOOH over *OCH_2O or *O & CH_2O (Fig. 5 and 6). This suggests that the Fe_2DOBDC and Fe_2-DSBDC clusters should selectively yield HCOOH as the only $2e^-$ reduced CO_2 product, as the formation of *OCOH is highly disfavored, hindering the formation of CO. While the reduction of CO_2 proceeds similarly on the Fe_2DOBDC and Fe_2DSBDC clusters, the binding of *HCOOH to the Fe sites differs significantly. On Fe_2DOBDC, the binding of *HCOOH is favorable by −0.07 eV, indicating that *HCOOH may remain adsorbed to the site and undergo further reduction. Conversely, the Fe_2DSBDC cluster results in a *HCOOH binding energy of 0.14 eV. A positive binding energy suggests that the *HCOOH intermediate is unlikely to remain adsorbed to the surface and should instead form as the sole product of CO_2 reduction. This trend may result from the less favorable van der Waals interaction due to the larger S atoms or the greater electron delocalization from the Fe–S bonds, aiding in more facile electron transport while lowering the affinity of the closed-shell adsorbates to the Fe site.

Examining subsequent PCET steps involving the adsorbed *HCOOH intermediate on the Fe_2DOBDC cluster, the most favorable intermediate to form is *OH, accompanied by the release of free CH_2O (Fig. 5). This reaction step includes the reduction of the C atom and the subsequent breaking of the C–O bond. A modest input of energy (0.07 eV) compared to the first PCET step (1.14 eV) is required and ultimately leads to the formation of H_2O following an additional PCET step. Notably, the *OH intermediate exhibits strong binding to the Fe site (−2.87 eV), reducing the likelihood of further reduction of CH_2O. The weak but favorable binding of *HCOOH to the Fe site in Fe_2DOBDC, combined with the nearly facile formation of *OH, suggests that CO_2 reduction is likely to result in the formation of both HCOOH and CH_2O on the Fe_2DOBDC MOF. This trend differs from our previous work,[15] but we believe that the different solvent environments and a more refined cluster model help stabilize the *OH intermediate, limiting further reduction to CH_4.

3.4 CO reduction reaction (CORR)

To gain deeper insights into the impact of S atom substitution on electrocatalytic reduction reactions within the MOF-74 framework, we extend our investigation beyond CO_2 reduction to explore the reduction of CO, potentially yielding a range of products beyond HCOOH and CH_2O. The binding of CO to the Fe site is notably stronger on the Fe_2DOBDC cluster, exceeding that on Fe_2DSBDC by 0.34 eV, a trend reminiscent of what we observed with both CO_2 and HCOOH. Additionally, a more pronounced charge accumulation is observed for CO on the Fe_2DOBDC cluster (−0.17) compared to the Fe_2DSBDC (−0.12). Furthermore, upon CO adsorption to the Fe_2DOBDC cluster, the CO stretching frequency experiences a red-shift of 285.7 cm^{-1}, while the weaker binding on the Fe_2DSBDC cluster results in a smaller red-shift of 231.0 cm^{-1}. These trends underscore the distinct influence of the ligand on CO adsorption to the respective Fe-sites.

The most thermodynamically favorable pathway for CO reduction on both clusters mirrors each other. Unlike CO_2 reduction, where a pattern of alternating C and O reduction leads to the formation of either HCOOH or CH_2O, CO reduction exhibits a consistent pattern, culminating in the complete reduction of the C atom to CH_4 followed by the subsequent reduction of the resulting O atom to form H_2O (Fig. S6†). The intermediates in this pathway include *CO, *HCO, *CH_2O, *CH_3O, *O, *OH, *H_2O.

The disparities between the Fe_2DOBDC and Fe_2DSBDC clusters results in significant differences in the energetics of CO reduction (Fig. 7 and 8). The initial reduction of *CO to *HCO yields limiting potentials of 1.18 eV and 0.62 eV for Fe_2-DOBDC and Fe_2DSBDC, respectively. This substantial difference in limiting potentials for CO reduction on the two clusters (0.56 eV) surpasses that observed for CO_2 reduction (0.12 eV), emphasizing the distinct electrocatalytic capabilities of these materials. Moreover, a subsequent PCET step yielding *CH_2O results in significant differences in binding to the Fe sites. On Fe_2DOBDC, the *CH_2O intermediate exhibits favorable binding with a ΔG value of −0.11 eV, while the same intermediate results in unfavorable binding equal to 0.25 eV

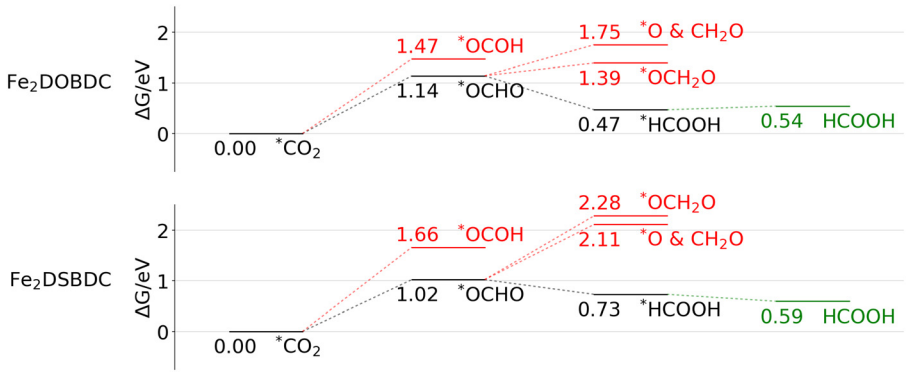

Fig. 6 Free energy profile for the reduction of CO_2 to HCOOH on the Fe_2DOBDC (top) and Fe_2DSBDC (bottom) clusters. All energy values are relative to *CO_2 for each respective cluster. Color code – favorable reduction (black), unfavorable reduction (red), desorption (green).

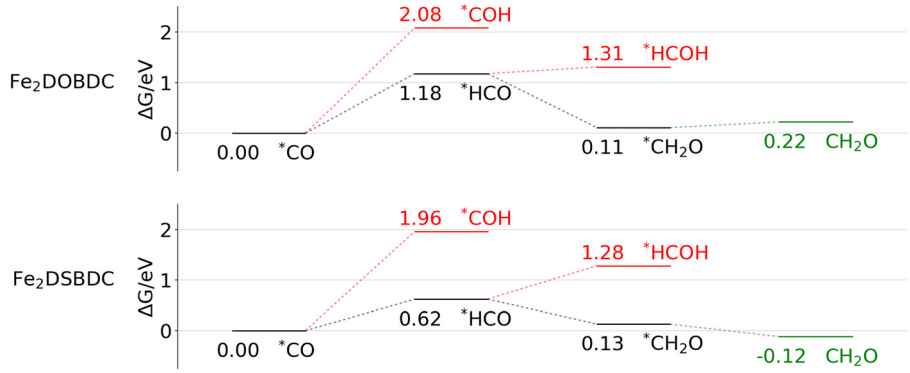

Fig. 7 Free energy profile for the reduction of CO to CH_2O on the (top) Fe_2DOBDC and (bottom) Fe_2DSBDC clusters. All energy values are relative to *CO for each respective cluster. Color code – favorable reduction (black), unfavorable reduction (red), desorption (green).

on Fe_2DSBDC. This strong desorption quality of the $*CH_2O$ intermediate on Fe_2DSBDC suggests that further reduction is improbable, indicating a high selectivity for CH_2O formation. Conversely, the Fe_2DOBDC cluster results in favorable binding for all of the reduced intermediates, ultimately leading to the favorable formation of CH_4 and H_2O following six PCET steps (Fig. 8). Hence, distinct product distributions for CO reduction on Fe_2DOBDC and Fe_2DSBDC clusters are anticipated, driven by the the binding of $*CH_2O$ to the Fe site.

4 Conclusions

Our investigation into the electrocatalytic reduction reactions on Fe-MOF-74 clusters, with and without S-substitution, has uncovered substantial behavioral differences. Earlier experimental work highlighted enhanced electrical conductivity upon replacing the DOBDC ligand with DSBDC, credited to the introduction of the heavier S atoms. Despite retaining the same topological structure, the S atoms in Fe_2-DSBDC induce distinct electronic structure variances compared to Fe_2DOBDC. The nature of the equatorial O atoms of Fe_2DOBDC result in stronger binding of the closed-shell reduction products, leading to the formation of deeper reduction products (CH_2O and CH_4) during CO_2 and CO reduction, respectively. Conversely, the larger and less electronegative equatorial S atoms of Fe_2DSBDC lead to weakened interactions with closed-shell reduction products, yielding only $2e^-$ products (HCOOH and CH_2O). These differences do not seem to affect the reduction of hydrogen, however, which resulted in nearly identical limiting potentials between the two systems. Our findings suggest the potential for engineering other MOFs by manipulating metal–ligand interactions, offering insights into tailoring catalysts for selective electrochemical transformations.

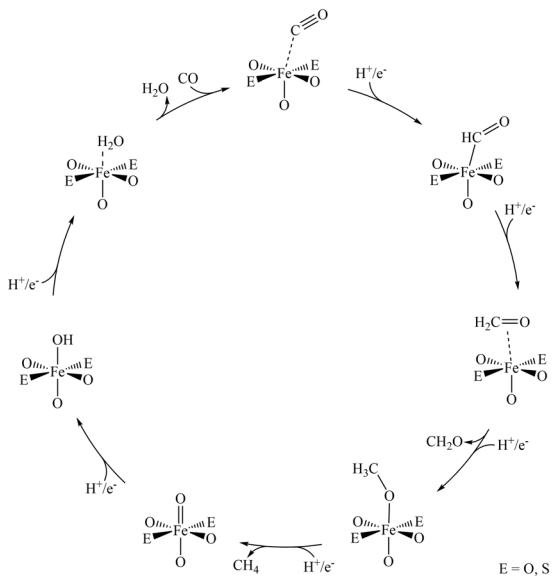

Fig. 8 Mechanistic cycle for the reduction of CO to CH_2O and CH_4. E = O or S for Fe_2DOBDC or Fe_2DSBDC, respectively.

Author contributions

G. A. M.: conceptualization, data curation, formal analysis, investigation, methodology, software, validation, visualization, writing – original draft; T. Y. and W. Z.: project administration, resources, supervision.[42]

Conflicts of interest

There are no conflicts to declare.

Acknowledgements

G. A. M. would like to thank NIST's Postdoctoral Program for an NRC Postdoctoral Fellowship and Morgan Kramer for insightful discussions around this work.

Notes and references

1 M. Yousaf, M. Zaman, A. Mahmood, M. Imran, A. Elkamel, M. Rizwan, T. Wilberforce and F. Riaz, *Energy Sci. Eng.*, 2022, **10**, 4890–4923.
2 M. He, S. Piao, C. Huntingford, H. Xu, X. Wang, A. Bastos, J. Cui and T. Gasser, *Commun. Earth Environ.*, 2022, **3**, 160.

3 J. S. Sperry, M. D. Venturas, H. N. Todd, A. T. Trugman, W. R. L. Anderegg, Y. Wang and X. Tai, *Proc. Natl. Acad. Sci. U. S. A.*, 2019, **116**, 25734–25744.
4 S. Nitopi, E. Bertheussen, S. B. Scott, X. Liu, A. K. Engstfeld, S. Horch, B. Seger, I. E. L. Stephens, K. Chan, C. Hahn, J. K. Nørskov, T. F. Jaramillo and I. Chorkendorff, *Chem. Rev.*, 2019, **119**, 7610–7672.
5 W. Ma, X. He, W. Wang, S. Xie, Q. Zhang and Y. Wang, *Chem. Soc. Rev.*, 2021, **50**, 12897–12914.
6 B. Ruqia, G. M. Tomboc, T. Kwon, J. Kundu, J. Y. Kim, K. Lee and S.-I. Choi, *Chem Catal.*, 2022, **2**, 1961–1988.
7 C. Li, H. Zhang, M. Liu, F.-F. Lang, J. Pang and X.-H. Bu, *Ind. Chem. Mater.*, 2023, **1**, 9–38.
8 Q. Wang and D. Astruc, *Chem. Rev.*, 2019, **120**, 1438–1511.
9 L. S. Xie, G. Skorupskii and M. Dincă, *Chem. Rev.*, 2020, **120**, 8536–8580.
10 R. Shah, S. Ali, F. Raziq, S. Ali, P. M. Ismail, S. Shah, R. Iqbal, X. Wu, W. He, X. Zu, A. Zada, Adnan, F. Mabood, A. Vinu, S. H. Jhung, J. Yi and L. Qiao, *Coord. Chem. Rev.*, 2023, **477**, 214968.
11 L. Sun, C. H. Hendon, M. A. Minier, A. Walsh and M. Dincă, *J. Am. Chem. Soc.*, 2015, **137**, 6164–6167.
12 G. Fu, A. Polity, N. Volbers, B. K. Meyer, B. Mogwitz and J. Janek, *Appl. Phys. Lett.*, 2006, **89**(26), 262113.
13 S. Ali, P. M. Ismail, F. Wahid, A. Kumar, M. Haneef, F. Raziq, S. Ali, M. Javed, R. U. Khan, X. Wu, H. Xiao, G. Yasin, L. Qiao and H. Xu, *Fuel Process. Technol.*, 2022, **236**, 107427.
14 S. Ali, P. M. Ismail, M. Humayun, M. Bououdina and L. Qiao, *Fuel Process. Technol.*, 2024, **255**, 108049.
15 G. A. McCarver, T. Yildirim and W. Zhou, *ChemPhysChem*, 2023, **24**(24), e202300645.
16 K. Li and D. Xue, *J. Phys. Chem. A*, 2006, **110**, 11332–11337.
17 R. G. Pearson, *J. Am. Chem. Soc.*, 1963, **85**, 3533–3539.
18 K. E. Laidig and R. F. W. Bader, *J. Chem. Phys.*, 1990, **93**, 7213–7224.
19 D. J. Xiao, E. D. Bloch, J. A. Mason, W. L. Queen, M. R. Hudson, N. Planas, J. Borycz, A. L. Dzubak, P. Verma, K. Lee, F. Bonino, V. Crocellà, J. Yano, S. Bordiga, D. G. Truhlar, L. Gagliardi, C. M. Brown and J. R. Long, *Nat. Chem.*, 2014, **6**, 590–595.
20 T. Van Phuc, S. G. Kang, J. S. Chung and S. H. Hur, *Mater. Res. Bull.*, 2021, **138**, 111228.
21 I. Choi, Y. E. Jung, S. J. Yoo, J. Y. Kim, H.-J. Kim, C. Y. Lee and J. H. Jang, *J. Electrochem. Sci. Technol.*, 2017, **8**, 61–68.
22 E. E. Benson, C. P. Kubiak, A. J. Sathrum and J. M. Smieja, *Chem. Soc. Rev.*, 2009, **38**, 89–99.
23 G. A. McCarver, T. Rajeshkumar and K. D. Vogiatzis, *Coord. Chem. Rev.*, 2021, **436**, 213777.
24 P. Verma, K. D. Vogiatzis, N. Planas, J. Borycz, D. J. Xiao, J. R. Long, L. Gagliardi and D. G. Truhlar, *J. Am. Chem. Soc.*, 2015, **137**, 5770–5781.
25 G. McCarver, T. Yildirim and W. Zhou, *Phys. Chem. Chem. Phys.*, 2024, **26**, 7627–7637.
26 Y. Zhao and D. G. Truhlar, *J. Chem. Phys.*, 2006, **125**, 194101.
27 S. Grimme, J. Antony, S. Ehrlich and H. Krieg, *J. Chem. Phys.*, 2010, **132**, 154104.
28 F. Neese, F. Wennmohs, U. Becker and C. Riplinger, *J. Chem. Phys.*, 2020, **152**, 224108.
29 F. Weigend and R. Ahlrichs, *Phys. Chem. Chem. Phys.*, 2005, **7**, 3297.
30 J. Kalinowski, F. Wennmohs and F. Neese, *J. Chem. Theory Comput.*, 2017, **13**, 3160–3170.
31 F. Weigend, *Phys. Chem. Chem. Phys.*, 2006, **8**, 1057–1065.
32 V. Barone and M. Cossi, *J. Phys. Chem. A*, 1998, **102**, 1995–2001.
33 A. V. Marenich, S. V. Jerome, C. J. Cramer and D. G. Truhlar, *J. Chem. Theory Comput.*, 2012, **8**, 527–541.
34 T. Lu and F. Chen, *J. Comput. Chem.*, 2012, **33**, 580–592.
35 J. Pipek and P. G. Mezey, *J. Chem. Phys.*, 1989, **90**, 4916–4926.
36 G. Knizia, *J. Chem. Theory Comput.*, 2013, **9**, 4834–4843.
37 G. Knizia and J. E. M. N. Klein, *Angew. Chem., Int. Ed.*, 2015, **54**, 5518–5522.
38 S. Grimme, *Chem. – Eur. J.*, 2012, **18**, 9955–9964.
39 R. Tyburski, T. Liu, S. D. Glover and L. Hammarström, *J. Am. Chem. Soc.*, 2021, **143**, 560–576.
40 G.-G. Luo, H.-L. Zhang, Y.-W. Tao, Q.-Y. Wu, D. Tian and Q. Zhang, *Inorg. Chem. Front.*, 2019, **6**, 343–354.
41 A. A. Peterson, F. Abild-Pedersen, F. Studt, J. Rossmeisl and J. K. Nørskov, *Energy Environ. Sci.*, 2010, **3**, 1311–1315.
42 E. Boutin, L. Merakeb, B. Ma, B. Boudy, M. Wang, J. Bonin, E. Anxolabéhère-Mallart and M. Robert, *Chem. Soc. Rev.*, 2020, **49**, 5772–5809.

